

# Wavelength-driven photoelectron momentum tilt in XUV Ionization

Neha Kukreti <sup>1</sup> and Amol R. Holkundkar <sup>1,\*</sup>

<sup>1</sup>*Department of Physics, Birla Institute of Technology and Science Pilani,  
Pilani Campus, Vidya Vihar, Pilani, Rajasthan 333031, India*

(Dated: May 14, 2026)

We investigate how atomic structure influences photoelectron momentum distributions (PMDs) in single-photon ionization by a linearly polarized extreme-ultraviolet (XUV) pulse. We demonstrate that the PMD tilt is governed not only by the magnetic quantum number but also by the radial structure of the bound atomic orbital. While neon exhibits a smooth wavelength dependence of the PMD tilt, argon displays a non-monotonic behavior characterized by suppression and reversal of the tilt at a critical wavelength. A partial-wave analysis reveals that this behavior arises from interference between  $s$ - and  $d$ -wave channels, with the reversal originating from a minimum in the  $d$ -wave radial dipole matrix element induced by the radial node in the argon  $3p$  orbital. We further show that atomic interferometric circular dichroism (AICD) serves as a sensitive probe of this effect. These findings establish a direct link between the radial wavefunction structure and observable momentum-space asymmetries, highlighting the wavelength-dependent rotation and the suppression of the PMD tilt as signatures of radial-node-induced Cooper-like suppression in the  $d$ -wave channel of argon.

## I. INTRODUCTION

Photoelectron momentum distributions (PMDs) provide a powerful window into the dynamics of light-matter interactions and have emerged as a central observable in attosecond and ultrafast physics [1–4]. By resolving the angular and energy distributions of emitted electrons, PMDs encode detailed information about both the driving laser field and the structure of the initial bound state [5–8]. In particular, the interplay between field polarization and electronic angular momentum leads to rich angular features that can be used to probe symmetry, phase, and interference effects at the quantum level [9–16].

A key aspect governing PMDs is the transfer of angular momentum from the field to the electron. For circularly polarized fields, the light’s helicity directly imprints chirality on photoelectron emission, giving rise to circular dichroism and enabling the probing of chiral and magnetic properties of matter across different systems [17–21]. In contrast, linearly polarized fields, while lacking intrinsic chirality, can still generate nontrivial angular asymmetries when the initial state carries a nonzero magnetic quantum number  $m$  [22, 23]. In such cases, the dipole selection rule  $\Delta m = \pm 1$  dictates the accessible continuum channels, and the resulting PMD is often interpreted in terms of angular momentum conservation and interference between allowed partial-wave channels [24, 25].

Previous studies have shown that photoelectron momentum distributions can exhibit interference effects when generated by time-delayed extreme-ultraviolet (XUV) pulses [26]. These features arise from the coherent superposition of continuum wave packets emitted at different times and reflect the phase accumulated during ionization. In this context, it is natural to ask how such phase-dependent features are influenced by additional factors such as light polarization and atomic structure. In particular, it remains unclear whether PMD characteristics, often linked to angular-momentum se-

lection rules, are universal or carry signatures of the underlying atomic structure.

Within this framework, it is often assumed that the qualitative features of the photoelectron momentum distribution (PMD), such as the direction of angular asymmetry or angular offset (hereafter referred to as the PMD tilt), are primarily governed by the magnetic quantum number of the initial state. In particular, for atoms prepared in the same magnetic quantum number  $m$  and subjected to identical driving fields, one would expect similar emission patterns, largely independent of the specific atomic species. This expectation reflects the dominant role typically attributed to angular momentum selection rules in shaping the PMD.

In this work, we demonstrate that this assumption does not hold in general. By comparing the single-photon ionization of the current-carrying state ( $m = +1$ ) of neon and argon using a linearly polarized XUV pulse, we observe a striking and counterintuitive behavior. Despite identical initial-state symmetry and driving conditions, the resulting PMDs exhibit opposite tilts at certain wavelengths.

This unexpected result reveals that angular momentum considerations alone are insufficient to fully describe the PMD, and points to a crucial role of atomic structure. It therefore raises a fundamental question: what determines the direction and magnitude of the PMD tilt? In particular, how does the internal structure of the atom influence the angular distribution of emitted electrons beyond the constraints imposed by selection rules?

To address this, we perform a detailed analysis based on numerical solutions of the full-dimensional time-dependent Schrödinger equation (TDSE) within the single-active-electron (SAE) approximation, complemented by a partial-wave decomposition of the continuum wavefunction. This approach enables us to identify the dominant angular-momentum channels and elucidate the interference mechanisms underlying the observed asymmetry.

Our results show that the PMD is primarily governed by interference between the  $s$ - and  $d$ -wave channels, with the tilt being sensitively dependent on their relative phase. While both neon and argon exhibit such interference, their behavior

\* amol@holkundkar.in

differs markedly as a function of the driving wavelength. In particular, argon displays a pronounced non-monotonic evolution of the tilt, including suppression and reversal at a critical wavelength, whereas neon exhibits a smooth and monotonic variation without reversal.

To further elucidate the physical origin of this effect and provide an experimentally accessible signature, we also introduce an interferometric scheme based on atomic-interferometric circular dichroism (AICD) [27]. By applying a weak circularly polarized probe pulse following the initial linearly polarized excitation, we show that the resulting dichroic signal provides direct access to the underlying partial-wave interference and its wavelength dependence. This approach offers a practical route to detect radial-node-induced effects and to identify magnetic sublevel contributions in photoionization experiments. Our results reveal the sensitivity of the angular features in photoelectron momentum distributions to the radial structure of atomic orbitals. More broadly, they demonstrate that PMDs encode not only angular-momentum selection rules but also detailed information about radial wavefunction structure, opening new possibilities for probing electronic structure via ultrafast photoionization.

The remainder of this paper is organized as follows. In Sec. II, we describe the theoretical framework and numerical method. The results are presented in Sec. III. Finally, Sec. IV summarizes the main conclusions. Additional detail is given in Appendix A.

## II. THEORETICAL AND NUMERICAL CONSIDERATIONS

We employ a full-dimensional time-dependent Schrödinger equation (TDSE) solver within the single-active-electron (SAE) approximation, implemented using the time-dependent generalized pseudospectral (TDGPS) method [26, 28–31]. In the length gauge, the TDSE takes the form:

$$i \frac{\partial}{\partial t} |\psi(\mathbf{r}, t)\rangle = [H_0 + H_L(t)] |\psi(\mathbf{r}, t)\rangle, \quad (1)$$

where  $H_0 = -\nabla^2/2 + V(r)$  denotes the field-free Hamiltonian, and  $H_L(t) = -\mathbf{r} \cdot \mathbf{E}(t)$  represents the laser-atom interaction in the length gauge. All quantities are expressed in atomic units ( $|e| = m_e = \hbar = 1$ ) throughout the manuscript.

The driving laser field is constructed using a vector-potential formulation, which ensures numerical stability for ultrashort pulses. The electric field is obtained as  $\mathbf{E}(t) = -\partial \mathbf{A}(t)/\partial t$ . To allow for a unified description of different pulse configurations (linear, circular, and their combinations), we express the total vector potential as a superposition of two time-delayed components,

$$\mathbf{A}(t) = \mathbf{A}_1(t) + \mathbf{A}_2(t - \tau), \quad (2)$$

where  $\tau$  is the interpulse delay. The first pulse  $\mathbf{A}_1(t)$  is chosen to be linearly polarized along the  $x$ -axis,

$$\mathbf{A}_1(t) = A_0 f(t) \sin(\omega_0 t) \hat{\mathbf{x}}, \quad (3)$$

while the second pulse  $\mathbf{A}_2(t - \tau)$  represents a circularly polarized field in the  $x - y$  plane,

$$\mathbf{A}_2(t - \tau) = \kappa \frac{A_0}{\sqrt{2}} f(t - \tau) [\cos(\omega_0(t - \tau)) \hat{\mathbf{x}} + \xi \sin(\omega_0(t - \tau)) \hat{\mathbf{y}}], \quad (4)$$

where  $\xi = \pm 1$  corresponds to left- and right-circular polarization, respectively. Here,  $A_0 = E_0/\omega_0$  is the peak vector potential amplitude,  $\omega_0$  is the carrier frequency. The pulse envelope is chosen as a  $\sin^2$  function,  $f(t) = \sin^2(\pi t/T)$ . The pulse duration is taken as  $T = 20 \tau_0$ , where  $\tau_0 = 2\pi/\omega_0$  is the optical cycle for the respective wavelength. This second delayed circularly-polarized pulse is only used while calculating the AICD with delay  $\tau = 3\tau_0$ , where  $\kappa = |\mathbf{A}_2|/|\mathbf{A}_1| = 0.5$  represents the relative strength of the probe beam to treat the probing perturbatively.

The peak electric field amplitude is related to the laser intensity  $I_0$  (in  $\text{W}/\text{cm}^2$ ) as

$$E_0 [\text{a.u.}] \simeq 5.342 \times 10^{-9} \sqrt{I_0}. \quad (5)$$

In the present work, the peak intensity is scaled with the atomic target and wavelength according to

$$I_0 = 1.0 \times 10^{14} \left( \frac{I_P}{0.7933} \right) \left( \frac{40.0}{\lambda} \right)^2, \quad (6)$$

where  $I_P$  is the ionization potential (in atomic units) of the target atom and  $\lambda$  (in nm) is the wavelength of the driving XUV pulse. This combined scaling ensures that the Keldysh parameter,  $\gamma \sim 26.8$ , remains approximately constant, maintaining identical ionization conditions across different atomic species (Ar and Ne) and wavelengths.

The atomic potential  $V(r)$  is modeled within the single-active-electron (SAE) approximation using an empirical form proposed in Ref. [32], with parameters for neon and argon taken from the same reference. This potential, based on self-interaction-free density functional theory, reproduces the Coulomb singularity without the need for soft-core regularization. Within the TDGPS method, the radial domain is mapped to a finite interval and discretized using Legendre polynomials, excluding the singular point at the origin [29, 33, 34].

The eigenenergies  $E_{n\ell}$  and corresponding radial eigenfunctions  $R_{n\ell}(r)$  of the field-free Hamiltonian  $H_0$  are computed for each partial wave  $\ell$  prior to time propagation using the split-operator method [29]. The time-dependent wavefunction is then expanded in this basis as

$$\psi(\mathbf{r}, t) = \sum_{n,\ell,m} C_{n\ell m}(t) R_{n\ell}(r) Y_{\ell m}(\theta_r, \varphi_r), \quad (7)$$

where  $C_{n\ell m}(t)$  are the time-dependent expansion coefficients describing the population dynamics; however,  $\theta_r$  and  $\varphi_r$  represent polar and azimuthal angles of the wavefunction in the position basis. Hereafter, the polar and azimuthal angles  $\theta$  and  $\varphi$  (without suffix) will be associated with the wavefunction in momentum basis. The calculations are converged with  $\ell_{\text{max}} = 15$ , consistent with the single-photon ionization regime. Furthermore, the ionization potential for argon and neon are obtained to be  $I_P^{\text{Ar}} \sim 0.5797$  a.u. and  $I_P^{\text{Ne}} \sim 0.7933$

a.u. respectively using the given SAE potential under the TDGPS framework. For both argon and neon, the ground state  $2p$  and  $3p$  is chosen with magnetic quantum number  $m = +1$  unless otherwise stated.

To obtain converged photoelectron spectra, the wavefunction is further propagated after the end of the pulse for an additional duration  $T_{\text{prop}}$ , with a time step  $\delta t = \min(0.1, \tau_0/100)$ , where  $\tau_0 = 2\pi/\omega_0$  is the optical cycle associated with the respective XUV wavelength. The total propagation time is thus  $T_{\text{final}} = T_{\text{end}} + T_{\text{prop}}$ , with  $T_{\text{prop}}$  chosen sufficiently large (typically several tens of optical cycles) to ensure asymptotic convergence.

The final wavefunction  $\psi_{\text{final}}(\mathbf{r}, T_{\text{final}})$  is projected onto the continuum by applying a radial mask for  $r \geq r_0$ , with  $r_0 = 100$  a.u., such that

$$\psi_{\text{cont}}(\mathbf{r}) = M(r, r_0) \psi_{\text{final}}(\mathbf{r}, T_{\text{final}}), \quad (8)$$

where  $M(r, r_0) = [1 + \exp(-3(r - r_0))]^{-1}$ . This procedure suppresses bound-state contributions and removes regions where the SAE potential deviates from a pure Coulomb form.

The PMD is then obtained by projecting the continuum wavefunction  $\psi_{\text{cont}}$  onto hydrogenic Coulomb scattering states [26, 35]. Although the SAE potential deviates from a pure Coulomb form at short range, it retains the correct asymptotic behavior  $-1/r$ . At the large distances ( $r \gtrsim 100$  a.u.) where the projection is performed, this deviation contributes only a short-range phase and does not affect the momentum distribution. The differential ionization probability is given by

$$\frac{dP}{d\mathbf{k}} = |\langle \psi_k^{-C} | \psi_{\text{cont}} \rangle|^2, \quad (9)$$

where  $|\psi_k^{-C}\rangle$  are the Coulomb scattering states [35]. Throughout this manuscript, we have presented polar-angle-integrated PMDs in the  $x-y$  plane, not just at  $\theta = \pi/2$ .

All PMDs presented in this manuscript are shown in the  $p_x$ - $p_y$  plane and correspond to the polar-angle integrated yield over  $\theta \in [0, \pi]$  at fixed  $k = |\mathbf{k}|$ :

$$P(p_x, p_y) = \int_0^\pi \frac{dP}{d\mathbf{k}} \sin \theta d\theta. \quad (10)$$

The displayed distributions are normalized with respect to their maximum yield. Furthermore, the results have been benchmarked against the Volkov projection method [36, 37], which yields consistent results but is computationally more demanding.

### III. RESULTS AND DISCUSSION

This section is divided into different subsections. First, we investigate the origin of the tilt observed in PMDs using a single linearly polarized pulse. A partial-wave analysis together with a reduced model is presented to quantitatively understand the observed tilt. Followed by employing AICD, in which a left-circularly polarized (LCP) or right-circularly polarized (RCP) probe pulse is used to interrogate the tilt in the PMD produced by the linearly polarized pump pulse.

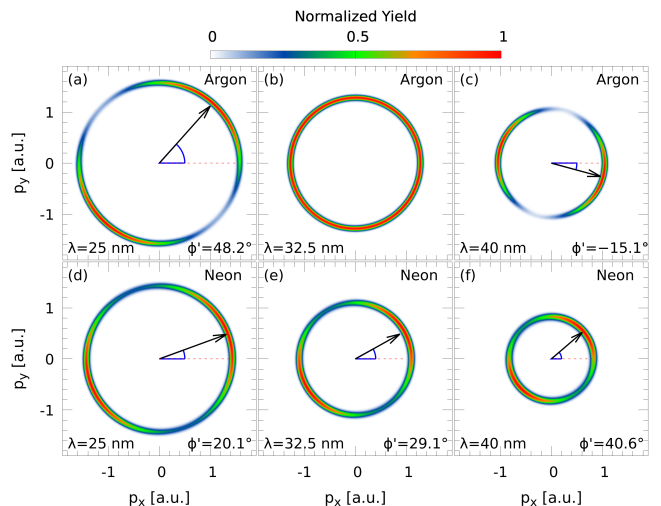


FIG. 1. Photoelectron momentum distributions (PMDs) in the  $p_x$ - $p_y$  plane for single-photon ionization of argon (top row) and neon (bottom row) at different wavelengths: (a,d)  $\lambda = 25$  nm, (b,e)  $\lambda = 32.5$  nm, and (c,f)  $\lambda = 40$  nm. The color scale represents the photoelectron yield normalized to its maximum value. The results are shown for the initial magnetic sublevel  $m = +1$ . The red dashed lines mark the reference polarization axis. The arrows mark the direction of maximum emission, and the corresponding angles  $\phi' \equiv \phi_{\text{max}}$ , quantify the tilt of the distribution.

#### A. Understanding PMD tilt through reduced partial-wave analysis

In Fig. 1, we show the PMDs for argon (top row) and neon (bottom row) subjected to a single linearly polarized (along  $\hat{x}$ ) XUV pulse, i.e.  $\mathbf{A}_1(t) \neq 0$  and  $\mathbf{A}_2(t) = 0$ . The results are presented for three different XUV wavelengths, namely  $\lambda = 25$ , 32.5, and 40 nm, while keeping the Keldysh parameter fixed as mentioned previously. The color scale represents the individually normalized photoelectron yield. For both atomic systems, the PMDs form a ring-like structure corresponding to single-photon ionization. However, a clear asymmetry in the angular distribution is observed, manifested as a tilt of the PMD with respect to the polarization axis. This tilt is quantified by the angle  $\phi_{\text{max}}$ , defined as the direction of maximum photoelectron yield from the polarization ( $\hat{x}$ ) axis.

A striking difference between argon and neon is immediately evident. In argon [Fig. 1(a)–(c)], the direction of the tilt changes with wavelength: at  $\lambda = 25$  nm the distribution is tilted in the positive direction ( $\phi_{\text{max}} = 48.2^\circ$ ), becomes nearly symmetric at  $\lambda = 32.5$  nm, and reverses its orientation at  $\lambda = 40$  nm ( $\phi_{\text{max}} = -15.1^\circ$ ). In contrast, neon [Fig. 1(d)–(f)] exhibits a monotonic increase in the tilt angle with wavelength, without any sign reversal. This qualitative difference indicates that the tilt is not solely determined by the magnetic quantum number of the initial state, which is identical in both cases ( $m = +1$ ), but depends sensitively on the atomic structure.

To gain deeper insight into the origin of the PMD structure and its atomic dependence, we analyze the photoelectron

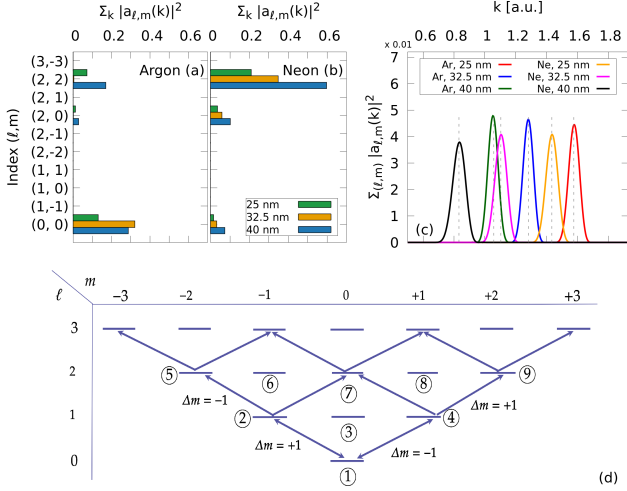


FIG. 2. Partial-wave analysis of the photoelectron continuum and its role in shaping the PMD. (a) Dominant angular-momentum channel contributions,  $\sum_k |a_{\ell,m}(k)|^2$ , for argon at different wavelengths. (b) Same as (a) for neon. In both cases, the continuum is dominated by a few channels, primarily  $(\ell, m) = (0, 0)$ ,  $(2, 0)$ , and  $(2, 2)$ , consistent with the dipole selection rule  $\Delta m = \pm 1$  for linearly polarized light. (c) Angle-integrated photoelectron momentum spectra,  $\sum_{\ell,m} |a_{\ell,m}(k)|^2$ , plotted as a function of electron momentum  $k$  for argon and neon at different wavelengths. (d) Schematic illustration of dipole-allowed transitions in the  $(\ell, m)$  manifold for linearly polarized light.

wavefunction in terms of its partial-wave decomposition. The continuum wavefunction  $\psi_{\text{cont}}(\mathbf{r})$  [refer Eq. (8)] is converted to momentum basis [12, 13, 35], and then expanded as:

$$\psi(\mathbf{k}) = \sum_{\ell,m} a_{\ell m}(k) Y_{\ell m}(\theta, \varphi). \quad (11)$$

Here,  $a_{\ell m}(k)$  represents the momentum-resolved amplitude of a given angular-momentum channel. The integrated channel contributions  $\sum_k |a_{\ell,m}(k)|^2$  for argon and neon, respectively, at different wavelengths are presented in Fig. 2(a) and Fig. 2(b), respectively. In both systems, only a few channels contribute significantly, namely  $(\ell, m) = (0, 0)$ ,  $(2, 0)$ , and  $(2, 2)$ . This dominance is a direct consequence of the dipole selection rule  $\Delta m = \pm 1$  for linearly polarized light. Starting from an initial state with  $m = +1$ , the allowed transitions populate only  $m = 0$  and  $m = 2$  channels, with the latter appearing only for  $\ell \geq 2$ .

The angle-integrated photoelectron momentum spectra, shown in Fig. 2(c), are obtained by summing over all partial-wave contributions,  $\sum_{\ell,m} |a_{\ell m}(k)|^2$ , and represent the quantity most directly accessible in typical experiments. The spectra exhibit well-defined peaks corresponding to single-photon ionization, with their positions governed primarily by energy conservation. In terms of the photoelectron momentum, this relation can be written as:

$$k \approx \sqrt{2(\omega - I_p)} \approx \sqrt{2 \left( \frac{45.563}{\lambda [\text{nm}]} - I_p \right)}. \quad (12)$$

where  $\lambda$  is the wavelength of XUV light and  $I_p$  is the ionization potential of the respective atomic species. In this frequency range, ponderomotive energy  $U_p \sim 10^{-4}$  a.u. and hence ignored in the energy conservation equation Eq. (12).

This systematic shift of the spectral maxima as predicted by Eq. (12) toward higher momenta with decreasing wavelength, in agreement with the trends observed in Fig. 2(c). The quantitative measure of the peak positions for argon ( $I_p \sim 0.5797$  a.u.) and neon ( $I_p \sim 0.7933$  a.u.) are offset due to their different ionization potentials, with neon consistently exhibiting lower momenta at a given wavelength. The overall spectral shapes remain qualitatively similar for both atomic systems. This demonstrates that angle-integrated observables are largely insensitive to the detailed atomic structure that governs the relative phase and amplitude of individual channels. In contrast, angle-resolved observables, such as the PMD tilt, provide a much more sensitive probe of the underlying angular-momentum composition and radial structure of the continuum.

Despite this common structure, a key difference emerges between the two atoms. For argon [Fig. 2(a)], the relative weight of the  $(2, 2)$  channel remains moderate compared to the  $(0, 0)$  and  $(2, 0)$  channels. In contrast, for neon [Fig. 2(b)], the  $(2, 2)$  contribution becomes significantly stronger, particularly at longer wavelengths. This difference directly impacts the interference strength responsible for the PMD asymmetry.

The physical origin of these dominant channels is summarized schematically in Fig. 2(d). For a linearly polarized field, which can be viewed as a superposition of left- and right-circularly polarized components, the dipole interaction enforces  $\Delta m = \pm 1$ . Consequently, the initial  $m = +1$  state couples to  $m = 0$  and  $m = 2$  channels through multiple pathways. These pathways form a network of interfering transitions connecting different  $(\ell, m)$  states. The final PMD is therefore governed by the coherent superposition of multiple quantum pathways, with the  $(2, 2)$  channel playing a central role in generating the azimuthal asymmetry.

As we observed in Fig. 2(a) and Fig. 2(b), the channels  $(\ell, m) = (0, 0)$ ,  $(2, 0)$ , and  $(2, 2)$  contribute predominantly. As a result, the continuum wavefunction given in Eq. (11) can be accurately approximated by the reduced form as:

$$\psi(\mathbf{k}) = \psi(k, \theta, \varphi) \approx a_{00}(k) Y_{00}(\theta, \varphi) + a_{20}(k) Y_{20}(\theta, \varphi) + a_{22}(k) Y_{22}(\theta, \varphi). \quad (13)$$

Using the factorization  $Y_{\ell m}(\theta, \varphi) = Y_{\ell m}^\theta(\theta) e^{im\varphi}$ , the above equation can be rewritten as:

$$\psi(k, \theta, \varphi) \approx A(k, \theta) + B(k, \theta) e^{i2\varphi}, \quad (14)$$

where

$$\begin{aligned} A(k, \theta) &= a_{00}(k) Y_{00}^\theta(\theta) + a_{20}(k) Y_{20}^\theta(\theta), \\ B(k, \theta) &= a_{22}(k) Y_{22}^\theta(\theta). \end{aligned} \quad (15)$$

This reduced form shows that the PMD asymmetry arises from interference between the  $m = 0$  and  $m = 2$  channels when the initial state is  $m = +1$ . Importantly, the  $m = 0$  component contains contributions from both  $s$ - and  $d$ -waves, while

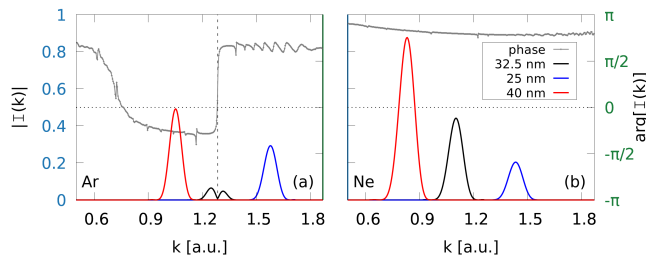


FIG. 3. Momentum-resolved interference term  $I(k)$  obtained from the partial-wave decomposition of the final wavefunction. The horizontal axis shows the electron momentum  $k$  (a.u.). The left vertical axis represents the magnitude  $|I(k)|$ , while the right vertical axis shows the phase  $\arg[I(k)]$  (for the 32.5 nm case). Panel (a) corresponds to argon and panel (b) to neon, for three driving wavelengths: 25 nm (blue), 32.5 nm (black), and 40 nm (red). The vertical dashed line in panel (a) marks  $k \approx 1.3$  a.u. ( $\sim 2.6$  Ry). The horizontal dotted line marks  $\arg[I(k)] = 0$ .

the  $m = 2$  component originates purely from the  $d$ -wave. The tilt therefore reflects the interference between these channels, with the  $s$ -wave contribution entering only through the  $m = 0$  component. Suppression of the  $d$ -wave channel therefore reduces the interference between  $m = 0$  and  $m = 2$  components, leading to a disappearance of the PMD tilt for argon with a 32.5 nm wavelength case [refer to Fig. 1(b) and Fig. 2(a)].

To further quantify this interference and its momentum dependence, we construct a momentum-resolved interference term  $I(k)$  from the dominant partial-wave amplitudes,

$$I(k) = a_{22}^*(k) [a_{00}(k) + a_{20}(k)]. \quad (16)$$

Here,  $I(k)$  represents the interference between the  $m = 2$  and  $m = 0$  channels arising from the dominant angular components. This quantity captures the interference between the  $s$ -wave and  $d$ -wave channels that govern the PMD asymmetry. Its magnitude  $|I(k)|$  reflects the strength of the interference, while the phase  $\arg[I(k)]$  directly determines the direction of the PMD tilt.

The momentum-resolved behavior of  $I(k)$  is presented in Fig. 3. For argon [Fig. 3(a)], a pronounced phase jump is observed near  $k \approx 1.3$  a.u. ( $\sim 2.6$  Ry) for the 32.5 nm case. This feature coincides with the Cooper-like minimum associated with the radial node of the  $3p$  orbital, where the dipole matrix element changes sign. As a consequence, the phase of  $I(k)$  undergoes an abrupt shift, leading to a reversal of the interference pattern and hence a change in the sign of the PMD tilt. Therefore, the phase behavior alone provides a direct indicator of whether the tilt is positive or negative. Though we have shown the phase for the 32.5 nm case only, this abrupt jump near  $k \approx 1.3$  a.u. is also observed for other wavelengths. In contrast, neon [Fig. 3(b)] exhibits a smooth variation of  $\arg[I(k)]$  across all wavelengths, with no abrupt phase discontinuity. This indicates that the relative phase between the contributing channels remains stable, and no sign reversal of the PMD tilt is expected. In the latter part, we will see that the observed differences between argon and neon can be traced back to the radial structure of the initial bound state.

## B. Quantifying PMD tilt

To quantify the angular tilt in the PMD, we rely on our reduced model. The angular distribution of the photoelectron yield is given by,

$$P(\varphi) = \int_0^\infty k^2 dk \int_0^\pi |\psi(k, \theta, \varphi)|^2 \sin \theta d\theta. \quad (17)$$

where,  $\psi(k, \theta, \varphi)$  is the approximated continuum electron wavefunction given by Eq. (14), and hence:

$$|\psi(k, \theta, \varphi)|^2 = |A|^2 + |B|^2 + 2\text{Re}[A^* B e^{i2\varphi}], \quad (18)$$

where,  $A(k, \theta)$  and  $B(k, \theta)$  correspond to the  $m = 0$  and  $m = 2$  contributions respectively.

After integration over  $k$  and  $\theta$ , the angular distribution reduces to

$$P(\varphi) = I_1 + I_2 + 2|V| \cos(2\varphi - \delta), \quad (19)$$

where  $I_1$  and  $I_2$  arise from  $|A|^2$  and  $|B|^2$ , and  $|V|e^{i\delta} = \int k^2 dk \int A^*(k, \theta) B(k, \theta) \sin \theta d\theta$  denotes the complex interference term after integration over  $k$  and  $\theta$ . The maximum of the distribution in Eq. (19) is simply given by:

$$\varphi_{\max} = \frac{\delta}{2}. \quad (20)$$

Thus, the PMD tilt angle  $\varphi_{\max}$  is determined solely by the relative phase between the dominant interfering channels. However, in the limit  $|V| \rightarrow 0$ , i.e., in the absence of the  $s$ - and  $d$ - channel interference, the PMD becomes azimuthally symmetric, leading to a disappearance of the tilt.

Figure 4(a) compares the angular distributions obtained from the full TDSE simulations and the reduced model for both argon and neon. The excellent agreement demonstrates that the PMD tilt is primarily governed by interference between the dominant partial waves, with higher-order channels playing a negligible role. This validates the reduced model as an effective framework for interpreting the underlying physics.

The dependence of the PMD tilt on the driving laser wavelength is presented in Fig. 4(b) and 4(c), which shows the PMD angular (polar) distributions for argon and neon, at wavelengths of 25 nm, 32.5 nm, and 40 nm. These angular distributions are fully consistent with the corresponding momentum-space PMDs shown in Fig. 1, confirming that the extracted tilt angle accurately captures the rotation of the emission pattern.

## C. Role of radial node in initial bound state and PMD tilt

As shown in Fig. 1 and Fig. 4, for neon, the PMD tilt increases monotonically with wavelength, indicating a smooth variation in the relative phase between the contributing partial waves. In contrast, argon exhibits a pronounced wavelength dependence, including a reversal of the tilt direction. Near

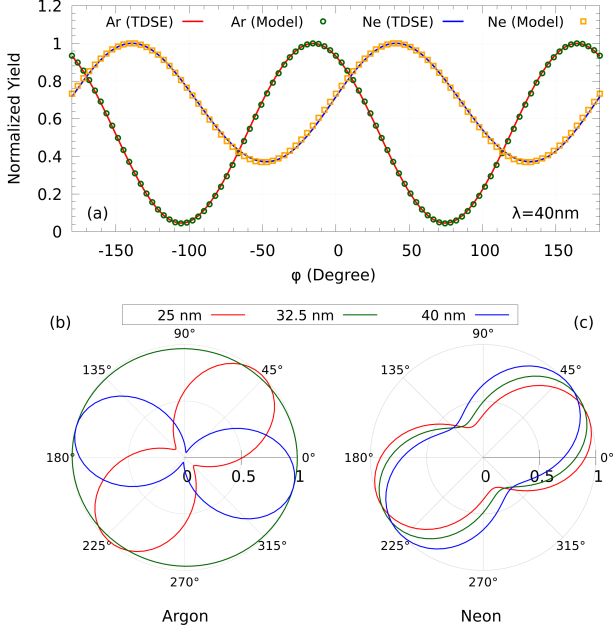


FIG. 4. (a) Comparison of the angular normalized photoelectron yield  $P(\varphi)$  obtained from full TDSE simulations (solid lines) and the reduced partial-wave model (symbols) for argon and neon at  $\lambda = 40$  nm. (b,c) Polar (angular) distributions of the normalized photoelectron yield for (b) argon and (c) neon at different driving wavelengths (25 nm, 32.5 nm, and 40 nm). The rotation of the angular distribution directly reflects the tilt of the PMD in momentum space. The extracted tilt angles are consistent with those obtained from the full PMDs (Fig. 1).

intermediate wavelengths (around 32.5 nm), the angular distribution becomes nearly symmetric, corresponding to a vanishing tilt.

This behavior can be traced to the radial structure of the initial bound state. It is well known that the argon in its ground state ( $3p$ ) possesses a radial node, whereas neon ( $2p$ ) does not [38]. The presence or the absence of the radial node can be quantified by the dipole transition amplitude from an initial bound state  $R_{np}(r)$  to a continuum state  $R_{k\ell}(r)$ , which is given as:

$$D_\ell(k) = \int_0^\infty R_{k\ell}(r) r R_{np}(r) dr, \quad (21)$$

here,  $R_{k\ell}(r)$  satisfies the field-free radial Schrödinger equation

$$H_0 R_{k\ell}(r) = \frac{k^2}{2} R_{k\ell}(r). \quad (22)$$

We can convert the momentum  $k$  of the continuum wavepacket in terms of the wavelength of the driving XUV pulse using energy conservation as:

$$\omega = I_p + \frac{k^2}{2}, \quad (23)$$

with the corresponding wavelength,

$$\lambda [\text{nm}] \approx \frac{45.563}{\omega [\text{a.u.}]}. \quad (24)$$

To establish a direct connection between the wavelength-dependent photoelectron angular distributions and the underlying atomic structure, we perform a systematic scan over the driving wavelength in the range 25–45 nm. The resulting angular distributions, dipole matrix elements, and extracted tilt angles are summarized in Fig. 5.

In Figs. 5(a) and 5(b), we present the wavelength-resolved angular distributions  $P(\varphi)$  for argon and neon, respectively. For argon, the angular distribution exhibits a pronounced and nontrivial evolution with wavelength. At shorter wavelengths, a clear angular modulation with a well-defined tilt is observed, indicating strong interference between the dominant outgoing partial waves. However, as the wavelength approaches  $\lambda \approx 32.5$  nm, the angular contrast is strongly suppressed, leading to an almost isotropic distribution in  $\varphi$ . Beyond this point, the angular modulation re-emerges with the opposite orientation, indicating a change in the sign of the tilt angle. This behavior is quantitatively captured in the extracted tilt angle  $\varphi_{\text{max}}$  shown as white markers in Fig. 5(a) and (b). The abrupt transition of  $\varphi_{\text{max}}$  from positive to negative values at  $\lambda \approx 32.5$  nm for argon corresponds to a relative phase jump between the interfering ionization channels, as seen in Fig. 3. At the transition point, the angular asymmetry vanishes, indicating a complete suppression of the interference contrast.

In contrast, neon [Fig. 5(b)] exhibits a qualitatively different behavior. The angular distribution remains well-defined across the entire wavelength range, with a smooth and continuous rotation of the emission pattern. The corresponding  $\delta$  parameter increases monotonically without any discontinuity or sign reversal, Fig. 5(b). This indicates that both the ampli-

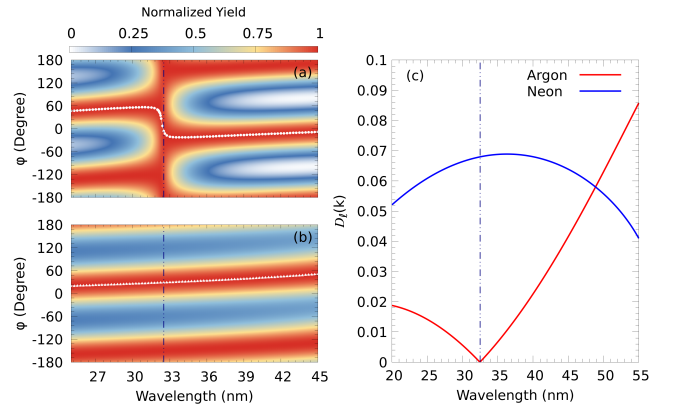


FIG. 5. Wavelength-resolved angular distributions and dipole matrix elements for single-photon ionization by a linearly polarized XUV pulse. (a) Angular distribution  $P(\varphi)$  as a function of wavelength  $\lambda$  for argon. (b) Same as (a) for neon. The color scale represents the normalized photoelectron yield. The vertical dashed line marks  $\lambda = 32.5$  nm. The white markers denote the extracted PMD tilt angles ( $\varphi_{\text{max}}$ ) over the wavelength range 25–45 nm. For argon, these points clearly show a transition from positive to negative tilt near  $\lambda \approx 32.5$  nm. In contrast, no such reversal is observed in neon, which exhibits a smooth, monotonic evolution. (c) Radial dipole matrix element  $D_\ell(k)$  (d-wave) as a function of wavelength for argon (red) and neon (blue). The results are obtained for an initial  $p$  state with magnetic quantum number  $m = +1$ .

tude and phase of the contributing ionization channels evolve smoothly with wavelength in neon.

In Fig. 5(c), we have shown the  $D_\ell(k)$  ( $d$ -wave) in terms of the driving XUV wavelength [Eq. (24)]. As can be seen in this figure, a pronounced minimum is observed in  $D_\ell(k)$  for argon near  $\lambda \approx 32.5$  nm, where the matrix element approaches zero. In contrast, the neon dipole matrix element remains finite and varies smoothly over the entire wavelength range. The suppression of  $D_\ell(k)$  in argon originates from the radial node in the initial  $3p$  orbital, as detailed. As evident from Eq. (21), the presence of a node leads to cancellation between contributions from different radial regions for a specific momentum  $k = k_{\min}$ , resulting in a strong suppression of the  $d$ -wave ( $\ell = 2$ ) channel.

The vanishing of the  $d$ -wave dipole matrix element has a direct consequence for the angular distribution. Since the observed PMD tilt arises from interference between partial waves, the suppression of the dominant  $d$ -wave channel leads to a collapse of the interference contrast, resulting in the disappearance of the tilt at  $\lambda \approx 32.5$  nm as shown in Fig. (1). As the wavelength increases further, the dipole matrix element changes sign across the minimum, leading to a phase shift in the relative phase between channels. This phase jump manifests as a reversal of the PMD tilt, as clearly seen in Fig. 5(a,b).

In neon, the absence of a radial node in the  $2p$  orbital prevents such cancellations in Eq. (21). Consequently, the dipole matrix element does not exhibit a minimum in the considered energy range, and both the amplitude and phase of the ionization channels evolve smoothly. This explains the continuous rotation of the angular distribution and the absence of any phase jump.

These results establish a direct and quantitative link between the radial structure of the initial bound state and the observable photoelectron angular distributions. The wavelength-resolved analysis demonstrates that the PMD tilt is governed not only by angular-momentum selection rules but also, critically, by the energy-dependent dipole matrix element and its associated phase. In particular, the radial-node-induced minimum in argon provides a clear, measurable signature, manifested as a suppression and reversal of the PMD tilt.

We also note that the suppression of  $D_\ell(k)$  at a particular XUV wavelength or photon energy closely resembles the ‘Cooper-Minimum’ associated with the radial node of the  $3p$  orbital [39]. However, in our case, this minimum ( $\sim 38$  eV or  $\sim 32.5$  nm) differs from experimentally established Cooper minima in argon, which occur near  $\sim 47$ – $49$  eV in photoionization measurements [40]. This disagreement with experimentally validated Cooper minima might be the manifestation of the approximate treatment of electron correlation and interchannel coupling [41–43]. Thus, the observed suppression in our case might be interpreted as a ‘Cooper-like’ minimum within the SAE framework. Despite this, the essential physics aspects, namely radial-node-induced suppression of the  $d$ -wave channel and its effect on the angular distributions of PMD, are correctly captured.

Furthermore, in Appendix-A, we also note that if the initial state is changed from  $m \rightarrow -m$ , the PMD tilt will be reversed

as expected. Accordingly, appropriate channels will be selected in accordance with the selection rule, without affecting the conclusions we draw from this study.

#### D. Atomic Interferometric Circular Dichroism

To establish a direct connection between the observed PMD asymmetries and experimentally accessible quantities, we analyze the atomic interferometric circular dichroism (AICD), defined as the difference between photoelectron yields generated by opposite probe helicities,  $\text{AICD} = (\text{LP} \rightarrow \text{LCP}) - (\text{LP} \rightarrow \text{RCP})$ . Here, ‘LP’ represents the linearly polarized pulse, which is followed by the delayed left (LCP) or right (RCP) circularly polarized light. The pulse configuration for AICD is represented by Eq. (2) with both  $\mathbf{A}_1(t) \neq 0$  and  $\mathbf{A}_2(t) \neq 0$ . The AICD isolates the helicity-dependent response of the ionization dynamics. Unlike the PMD tilt, which encodes phase information through a geometric rotation, AICD converts it into an intensity asymmetry, providing a more robust and experimentally accessible measure.

For all momentum distributions, the axes are scaled by  $p_\lambda$

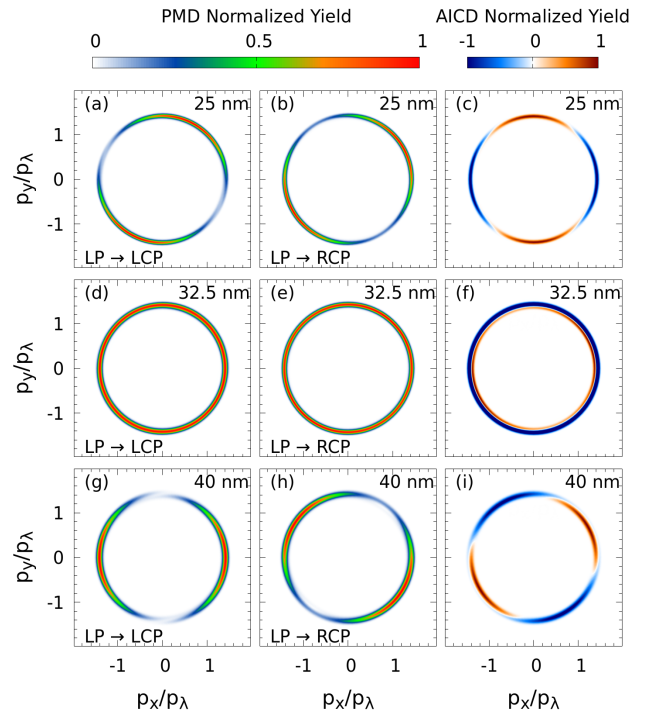


FIG. 6. Photoelectron momentum distributions (PMDs) and corresponding atomic interferometric circular dichroism (AICD) for argon. (a,d,g) PMDs for the LP  $\rightarrow$  LCP configuration and (b,e,h) PMDs for LP  $\rightarrow$  RCP at wavelengths 25 nm, 32.5 nm, and 40 nm, respectively. (c,f, i) Corresponding AICD distributions defined as  $\text{AICD} = (\text{LP} \rightarrow \text{LCP}) - (\text{LP} \rightarrow \text{RCP})$ . The PMDs are normalized to their maximum value, while the AICD is normalized to the peak dichroic contrast. The momentum axes are scaled by  $p_\lambda$ , such that the radial extent is identical for all wavelengths, enabling direct comparison of angular features.

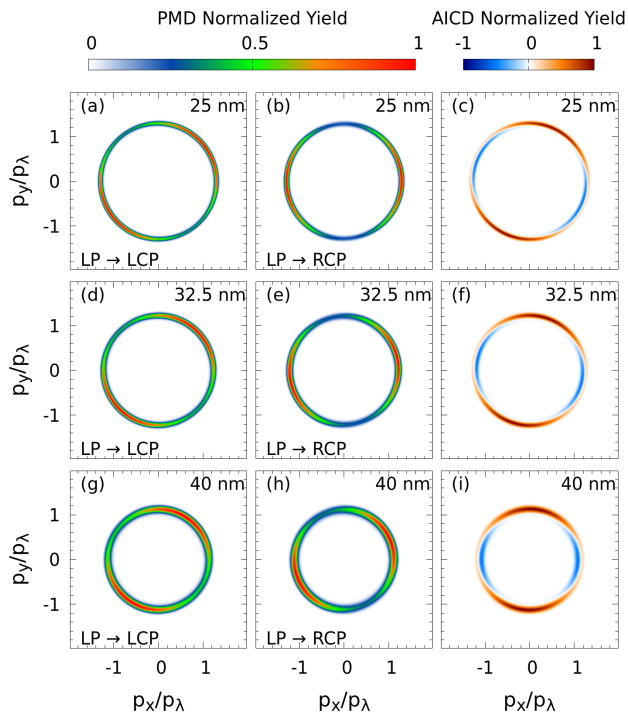


FIG. 7. Same as Fig. 6, but for neon. The momentum axes are scaled by  $p_\lambda$ , ensuring identical radial extent across wavelengths.

according to Eq. (12), ensuring identical radial extent across wavelengths and enabling direct comparison of angular features. Figures 6 and 7 show the AICD distributions for argon and neon, respectively, at wavelengths of 25 nm, 32.5 nm, and 40 nm, together with the corresponding PMDs. The results demonstrate that AICD directly reflects the magnetic quantum number of the initial state. Since the interference phase depends on the sign of  $m$ , reversing  $m \rightarrow -m$  leads to a corresponding inversion of the dichroic signal. Thus, the angular structure and sign of the AICD provide a clear signature of the underlying angular momentum.

A pronounced difference is observed between argon and neon in their wavelength dependence. In argon, the AICD exhibits a strong non-monotonic behavior. At 25 nm, the dichroic signal is well defined, indicating strong interference between partial waves. As the wavelength approaches 32.5 nm, the signal is strongly suppressed, reflecting a reduction of the interference contrast. At longer wavelengths, the AICD reappears with opposite sign, indicating a reversal of the underlying phase. This behavior is a direct consequence of the ‘Cooper-like’ minimum in argon, where the  $d$ -wave dipole matrix element is suppressed and undergoes a rapid phase shift at a certain driver wavelength. However, for  $\sim 32.5$  nm, the interference term vanishes, leading to the disappearance of the dichroic signal, whereas beyond this the phase reversal produces an inversion of the AICD pattern.

In contrast, neon exhibits a qualitatively different behavior. The AICD signal remains finite across the entire wavelength range and evolves smoothly without suppression or sign rever-

sal. This reflects the absence of a radial node in the  $2p$  orbital, leading to a smooth energy dependence of the dipole matrix elements and a continuous variation in the interference phase. These results highlight AICD’s sensitivity to both angular momentum and radial structure. While its existence is governed by selection rules, its magnitude and phase evolution are controlled by the energy dependence of the dipole matrix elements. From an experimental perspective, AICD provides a robust probe that can identify magnetic sublevels, distinguish co- and counter-rotating emissions, and reveal structural features such as Cooper-like minima. Its differential nature further reduces sensitivity to systematic uncertainties in absolute yields, making it well suited for momentum-resolved measurements such as velocity-map imaging [44] or COLTRIMS [45].

Overall, the AICD analysis establishes a direct link between partial-wave phase dynamics and measurable photoelectron asymmetries. In particular, it reveals a smooth, structure-insensitive response in neon, and a pronounced, non-monotonic behavior in argon driven by its radial nodal structure.

#### IV. CONCLUSION

We have investigated the origin of photoelectron momentum distribution (PMD) tilt in single-photon ionization by a linearly polarized extreme-ultraviolet (XUV) pulse, focusing on the role of atomic structure. Combining full-dimensional TDSE simulations within the single-active-electron (SAE) framework with a reduced partial-wave analysis, we show that the tilt arises from interference between a small set of dominant channels, primarily the  $m = 0$  and  $m = 2$  components associated with  $s$ - and  $d$ -wave contributions.

We demonstrate that the tilt is not determined solely by the magnetic quantum number, but is strongly influenced by the radial structure of the bound orbital through energy-dependent dipole matrix elements. Argon exhibits a pronounced non-monotonic behavior, including suppression and reversal of the tilt, whereas neon shows a smooth evolution. This contrast originates from the radial node in the argon  $3p$  orbital, which suppresses the  $d$ -wave dipole matrix element and induces a rapid variation of the relative phase between interfering channels, consistent with a Cooper-like minimum within the SAE description.

A wavelength-resolved analysis establishes a direct correspondence between the dipole matrix element and the PMD asymmetry: suppression of the  $d$ -wave channel reduces the interference contrast and eliminates the tilt, whereas its recovery, accompanied by a phase shift, reverses the emission direction. This provides a unified picture linking angular-momentum selection rules, radial structure, and observable momentum-space asymmetries.

We further show that atomic interferometric circular dichroism (AICD) provides a robust and experimentally accessible probe of this physics. The AICD signal reflects the same underlying interference but maps phase information onto an intensity asymmetry. In argon, it exhibits suppression

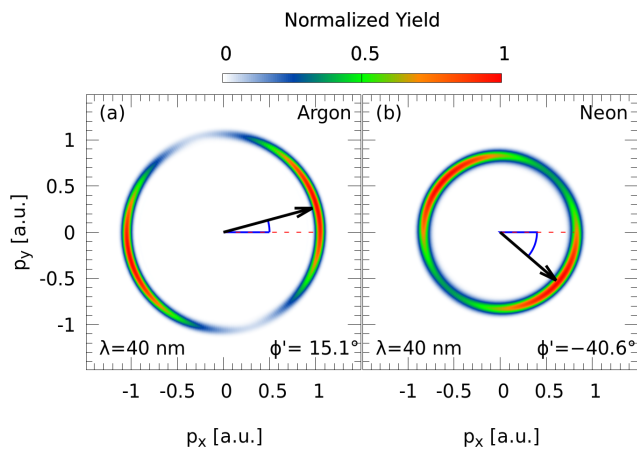


FIG. 8. Photoelectron momentum distributions (PMDs) for the initial state with magnetic quantum number  $m = -1$  for argon (a) and neon (b) at  $\lambda = 40$  nm. The tilt angle  $\phi'$  is indicated in each panel. In contrast to the  $m = +1$  case shown in Fig. 1, the PMD tilt reverses its direction for both argon and neon, while preserving its magnitude and overall structure.

and sign reversal across the dipole minimum, while in neon, it evolves smoothly, mirroring the PMD tilt behavior. This establishes AICD as a sensitive probe of both magnetic quantum number and radial-structure effects.

Overall, PMDs encode not only angular momentum transfer but also detailed information about the radial structure of atomic orbitals. The sensitivity of PMD tilt and AICD to channel-resolved interference highlights the potential of momentum-resolved photoelectron spectroscopy as a diagnostic tool for atomic and molecular structure.

## ACKNOWLEDGMENTS

The authors acknowledge the Department of Science and Technology (DST) for providing computational resources through the FIST program (Project No. SR/FST/PS-1/2017/30). Also, the authors acknowledge BITS - Pilani, Pilani Campus, for providing the ‘Jayant’ HPC facility.

## DATA AVAILABILITY

The data that support the findings of this article are not publicly available. The data are available from the authors upon reasonable request.

### Appendix A: Magnetic sublevel dependence of PMD Tilt

To verify the role of the initial-state magnetic quantum number, we present in Fig. 8 the photoelectron momentum distributions obtained for the  $m = -1$  state for both argon and neon. A direct comparison with the  $m = +1$  results shown in Fig. 1 reveals that the PMD tilt reverses its direction for all wavelengths and for both atomic species. This reversal originates from the change in the azimuthal phase structure of the initial state under the transformation  $m \rightarrow -m$ , which effectively corresponds to a mirror reflection of the angular distribution in the polarization plane. Importantly, while the tilt direction changes sign, its magnitude and the overall ring structure remain unchanged. This demonstrates that the interference mechanism responsible for the PMD asymmetry is robust and independent of the choice of magnetic sublevel, with the sign of the tilt determined solely by the relative phase between the contributing partial-wave channels.

- 
- [1] F. Krausz and M. Ivanov, *Rev. Mod. Phys.* **81**, 163 (2009).
  - [2] P. B. Corkum and F. Krausz, *Nat. Phys.* **3**, 381 (2007).
  - [3] M. Nisoli, P. Decleva, F. Calegari, A. Palacios, and F. Martín, *Chem. Rev.* **117**, 10760 (2017).
  - [4] P. B. Corkum, *Phys. Rev. Lett.* **71**, 1994 (1993).
  - [5] M. Lewenstein, P. Balcou, M. Y. Ivanov, A. L’Huillier, and P. B. Corkum, *Phys. Rev. A* **49**, 2117 (1994).
  - [6] A. T. J. B. Eppink and D. H. Parker, *Review of Scientific Instruments* **68**, 3477–3484 (1997).
  - [7] W. Becker, F. Grasbon, R. Kopold, D. Milošević, G. Paulus, and H. Walther (Academic Press, 2002) pp. 35–98.
  - [8] N. Douguet and K. Bartschat, *Phys. Rev. A* **106**, 053112 (2022).
  - [9] K.-J. Yuan, S. Chelkowski, and A. D. Bandrauk, *Phys. Rev. A* **93**, 053425 (2016).
  - [10] M.-H. Yuan and X.-B. Bian, *Phys. Rev. A* **101**, 013412 (2020).
  - [11] S. Kerbstadt, D. Pengel, D. Johannmeyer, L. Englert, T. Bayer, and M. Wollenhaupt, *New Journal of Physics* **19**, 103017 (2017).
  - [12] M. Murakami and S.-I. Chu, *Phys. Rev. A* **93**, 023425 (2016).
  - [13] M. Murakami, G. P. Zhang, and S.-I. Chu, *Phys. Rev. A* **95**, 053419 (2017).
  - [14] J.-P. Wang and F. He, *Phys. Rev. A* **95**, 043420 (2017).
  - [15] D. F. Dar and S. Fritzsche, *Phys. Rev. A* **109**, L041101 (2024).
  - [16] X.-B. Bian and A. D. Bandrauk, *Phys. Rev. Lett.* **108**, 263003 (2012).
  - [17] J. M. Ngoko Djiokap, S. X. Hu, L. B. Madsen, N. L. Manakov, A. V. Meremianin, and A. F. Starace, *Phys. Rev. Lett.* **115**, 113004 (2015).
  - [18] N. Bowering, T. Lischke, B. Schmidtke, N. Müller, T. Khalil, and U. Heinzmann, *Phys. Rev. Lett.* **86**, 1187 (2001).
  - [19] G. A. Garcia, L. Nahon, M. Lebeck, J.-C. Houver, D. Dowek, and I. Powis, *The Journal of Chemical Physics* **119**, 8781–8784 (2003).
  - [20] A. N. Artemyev, R. Tomar, D. Trabert, D. Kargin, E. Kutscher, M. S. Schöffler, L. P. H. Schmidt, R. Pietschnig, T. Jahnke, M. Kunitski, S. Eckart, R. Dörner, and P. V. Demekhin, *Phys. Rev. Lett.* **132**, 123202 (2024).
  - [21] T. Nakagawa, K. Watanabe, Y. Matsumoto, and T. Yokoyama, *Journal of Physics: Condensed Matter* **21**, 314010 (2009).
  - [22] J. J. Omiste and L. B. Madsen, *Journal of Physics B: Atomic, Molecular and Optical Physics* **54**, 054001 (2021).
  - [23] S. Chelkowski, A. D. Bandrauk, and P. B. Corkum, *Phys. Rev. A* **95**, 053402 (2017).

- [24] M.-X. Wang, X.-R. Xiao, H. Liang, S.-G. Chen, and L.-Y. Peng, *Phys. Rev. A* **96**, 043414 (2017).
- [25] B. Böning and S. Fritzsche, *Phys. Rev. A* **102**, 053108 (2020).
- [26] N. Kukreti and A. R. Holkundkar, *Phys. Rev. A* **113**, 053103 (2026).
- [27] S. McKay, H. B. Ambalampitiya, D. Peng, A. Saenz, and J. M. Ngoko Djiokap, *Phys. Rev. A* **111**, 053116 (2025).
- [28] X.-M. Tong and S.-I. Chu, *Chem. Phys.* **217**, 119 (1997).
- [29] X.-M. Tong, *J. Phys. B: At. Mol. Opt. Phys.* **50**, 144004 (2017).
- [30] A. R. Holkundkar, R. Rajpoot, and J. N. Bandyopadhyay, *Phys. Lett. A* **461**, 128645 (2023).
- [31] R. Rajpoot and A. R. Holkundkar, *J. Phys. B: At. Mol. Opt. Phys.* **56**, 105402 (2023).
- [32] X. M. Tong and C. D. Lin, *J. Phys. B: At. Mol. Opt. Phys.* **38**, 2593 (2005).
- [33] X.-M. Tong and S.-I. Chu, *Chem. Phys.* **217**, 119 (1997).
- [34] J. Wang, S.-I. Chu, and C. Laughlin, *Phys. Rev. A* **50**, 3208 (1994).
- [35] L. B. Madsen, L. A. A. Nikolopoulos, T. K. Kjeldsen, and J. Fernández, *Phys. Rev. A* **76**, 063407 (2007).
- [36] M. Murakami, O. Korobkin, and M. Horbatsch, *Phys. Rev. A* **88**, 063419 (2013).
- [37] M. Murakami and G.-P. Zhang, *Phys. Rev. A* **101**, 053439 (2020).
- [38] B. H. Bransden and C. J. Joachain, *Physics of atoms and molecules*, second edition. ed. (Prentice Hall, Harlow, 2003).
- [39] J. W. Cooper, *Phys. Rev.* **128**, 681 (1962).
- [40] J. Samson and W. Stolte, *Journal of Electron Spectroscopy and Related Phenomena* **123**, 265 (2002).
- [41] C. Alexandridi, D. Platzter, L. Barreau, D. Busto, S. Zhong, M. Turconi, L. Neoričić, H. Laurell, C. L. Arnold, A. Borot, J.-F. Hergott, O. Tcherbakoff, M. Lejman, M. Gisselbrecht, E. Lindroth, A. L’Huillier, J. M. Dahlström, and P. Salières, *Phys. Rev. Res.* **3**, L012012 (2021).
- [42] O. Hassouneh, N. B. Tyndall, J. Wragg, H. W. van der Hart, and A. C. Brown, *Phys. Rev. A* **98**, 043419 (2018).
- [43] M. Y. Amus’ya, N. A. Cherepkov, and L. V. Chernysheva, *Journal of Experimental and Theoretical Physics* **33**, 90 (1971).
- [44] A. T. J. B. Eppink and D. H. Parker, *Review of Scientific Instruments* **68**, 3477 (1997).
- [45] R. Dörner, V. Mergel, O. Jagutzki, L. Spielberger, J. Ullrich, R. Moshhammer, and H. Schmidt-Böcking, *Physics Reports* **330**, 95 (2000).